JACS
JOURNAL OF THE AMERICAN CHEMICAL SOCIETY
pubs.acs.org/JACS
Article

Oxoisoaporphine Alkaloid Iridium(III) Derivative: An Immunogenic Cell Death Inducer That Engages the Autophagy-Dependent Regulator Cathepsin D

Yuan Lu,[#] Feng-Yang Wang,[#] Matthew S. Levine,[#] Hai-Rong Shi, Yuan Wang, Xiaolin Xiong, Liang-Mei Yang, Ya-Qian Shi, Taotao Zou,* Jonathan L. Sessler,* Hong Liang,* and Ke-Bin Huang*

Cite This: J. Am. Chem. Soc. 2025, 147, 15216−15228
Read Online

ABSTRACT: Autophagy has been recognized as one of the pathways for eliciting immunogenic cell death (ICD). However, the specific molecular target responsible for autophagy-mediated ICD has not yet been elucidated. Here, we report that an oxoisoaporphine alkaloid-modified iridium(III) complex (**2a**) displays autophagy-inducing ICD activity. Through unbiased thermal proteome profiling (TPP), this new complex was found to interact with the lysosomal protease cathepsin D (Cat D). Subsequent cellular and biochemical assays—including the cellular thermal shift assay, isothermal dose-response assay, enzymatic assays, and molecular docking—confirmed that **2a** binds to and inhibits Cat D. Further pathway analysis demonstrated that **2a** triggers autophagy-dependent ICD via the LKB1-AMPK-ULK1 signaling pathway by inhibiting Cat D. Several other autophagy-dependent ICD inducers were tested and likewise found to inhibit Cat D. In contrast, an earlier reported analogue of **2a**, complex **1a**, was found to bind and destabilize binding immunoglobulin protein (BiP) and promote its ICD activity through an endoplasmic reticulum stress response. We believe that the findings reported here will enhance the understanding of the novel mechanisms of ICD agents and pave the way for the design of new ICD inducers with high specificity and efficacy.

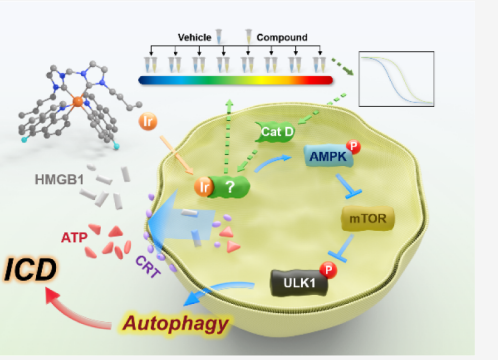

INTRODUCTION

Immunogenic cell death (ICD) is a regulated form of cell death that can activate a long-lasting adaptive antitumor immune response in immunocompetent hosts.[1,2] It is characterized by the elicitation of three major damage-associated molecular patterns (DAMPs),[3,4] which function as "biochemical hallmarks": (i) surface exposure of calreticulin (CRT), (ii) active secretion of adenosine triphosphate (ATP), and (iii) release of high mobility group protein 1 (HMGB1) from dying cells, as well likely other factors that have yet to be identified. Chemotherapy drugs typically target cancer through a "first hit" of cytotoxicity directed at cancer cells, followed by provoking the host's anticancer immunity as a "second hit".[5] Recent studies have disclosed that some ICD agents can enhance CAR-T cells to fight solid tumors by affecting the tumor microenvironment.[6,7] Moreover, some ICD inducers have been found to amplify synergistically the therapeutic effects of PD-1/PD-L1 blockade agents.[8−11] Clinical trials based on these finding are now ongoing.[12,13]

Several chemotherapeutic drugs in clinical use, including oxaliplatin (OXA), doxorubicin, cyclophosphamide, mitoxantrone (MTX), have all exhibited some degree of ICD.[12] Numerous reports on experimental platinum, iridium, gold, ruthenium, rhenium, manganese, and copper complexes that promote ICD-associated DAMPs have appeared recently.[14−48] However, only a limited subset are recognized as being bona fide ICD inducers as defined by an ability to prevent tumor growth in vivo under so-called challenge conditions where a treated animal is reinjected with fresh cancer cells (also referred to as a "vaccination effect"). Iridium complexes of which we are aware that demonstrate efficacy in this or analogous in vivo models are listed in Table S1. Collectively, these help underscore the promise of Ir complex-based ICD. Nevertheless, to our knowledge, as yet no pharmacophore directly responsible for ICD induction has been identified for the complexes in question. Doing so, could help advance the field.

Our group previously reported a cyclometalated Ir(III) complex (**1a**) as an ICD inducer. It was found to bind and destabilize binding immunoglobulin protein (BiP) and promote its ICD activity through an endoplasmic reticulum (ER) stress response.[33] Although some chemotherapeutic

Received: January 6, 2025
Revised: April 13, 2025
Accepted: April 15, 2025
Published: April 25, 2025

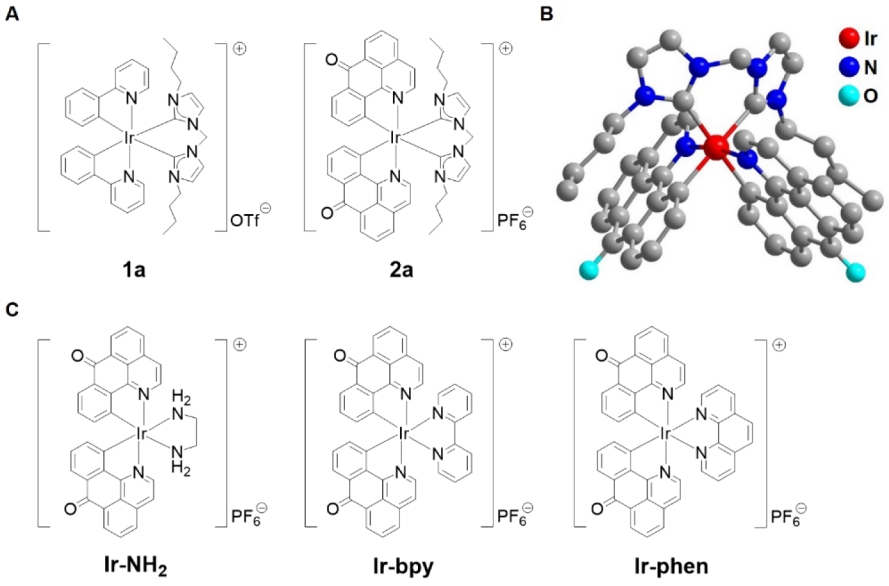

Figure 1. Chemical structures of Ir(III) complexes studied here. (A) Chemical structures of **1a** (reproduced from ref 51 with permission from the Royal Society of Chemistry) and **2a**. (B) X-ray crystal structure of **2a** (CCDC No. 2333613). (C) Chemical structures of **Ir-NH$_2$**, **Ir-bpy**, and **Ir-phen**.

agents elicit ICD through autophagy, not all autophagy-inducing agents can trigger an anticancer immune response.[49] Currently, the precise biotargets that initiate and sustain autophagy-mediated ICD remain largely unknown. We have thus sought to elucidate the target and mechanism behind autophagy-dependent ICD. We have done so using a new cyclometalated Ir(III) complex (**2a**) that incorporates an oxoisoaporphine alkaloid instead of the phenylpyridine ligand present in **1a** (Figure 1A). This design was inspired by an appreciation that synergistic effects are often seen between metal ions and bioactive alkaloid-based ligands.[50] As detailed below, we have found that **2a** induces the key hallmarks of ICD in vitro and provides a superior vaccination effect compared to OXA and **1a** in vivo. Of note, complex **2a** was not found to act through BiP. Based on the results of target profiling, cathepsin D (Cat D), a key protein that regulates autophagy, is proposed to underlie the ICD-inducing ability of **2a**. To the best of our knowledge, this is the first chemical−biological study revealing the proximate target of autophagy-dependent ICD. Preliminary experiments with other autophagy-dependent ICD agents lead us to suggest the general engagement of Cat D-related proteins as a basis for action.

RESULTS AND DISCUSSION

Synthesis and Characterization. In an effort to improve the ICD-related activity of **1a**, we synthesized a new cyclometalated Ir(III)-bis-NHC complex **2a** (Figure 1A). This was done by substituting the phenylpyridine moiety present in **1a** with an oxoisoaporphine alkaloid moiety while keeping the NHC ligand and metal center intact. The oxoisoaporphine ligand (L_a) was synthesized as previously reported,[52] while the bis-NHC ligand (L_b) was prepared through a one-pot reaction of 1-*n*-butyl-1*H*-imidazole with dibromomethane, using a modification of a published procedure (Scheme S1).[51] The synthetic route to **2a** is depicted in Scheme S2. In brief, the cyclometalated Ir(III) chloro-bridged dimer $[(L_a)_2Ir(\mu\text{-Cl})]_2$ was prepared by heating $IrCl_3{\cdot}3H_2O$ and L_a in a solution of 2-methoxyethanol (2-ME) and H_2O (3:1, v/v) at reflux. Complex **2a** was then obtained by subjecting $[(L_a)_2Ir(\mu\text{-Cl})]_2$ and ligand L_b to reflux in 2-ME in the presence of Ag_2O. The Supporting Information provides details of the synthesis of L_b and **2a**.

Ligand L_b and **2a** were characterized through $^1H/^{13}C$ NMR spectroscopy and ESI−MS (Figures S1−S6). Complex **2a** was found to be stable in TBS (Tris-KCl-HCl buffer, pH 7.35) for 48 h at room temperature (Figure S7). Additionally, **2a** was also characterized by single crystal X-ray diffraction analysis (Figure 1B and Table S2). The Ir(III) metal center adopts a distorted octahedral geometry with an equatorial coordination plane formed by the cis orientation of the metal−carbon bonds from ligands L_a and L_b, while the axial sites are occupied by N atoms from two L_a ligands in a trans arrangement. To compare the physicochemical properties of **1a** and **2a**, the octanol-water partition coefficient (log $P_{o/w}$), UV−vis absorption spectra, emission spectra, and cyclic voltammetry curves of **1a** and **2a** were analyzed. The log $P_{o/w}$ values of **1a** and **2a** are 1.81 and 3.50, respectively (Figure S8). Although, it may reflect a change in the counter anion, these values per se indicate that their lipophilicity is significantly different. The UV−vis spectra reveal distinct absorption maxima at 380 nm for **1a** and 510 nm for **2a** (Figure S9), demonstrating that the extended π-conjugation in the oxoisoaporphine ligand of **2a** induces a significant 130 nm bathochromic shift compared to the phenylpyridine-based **1a**. Additionally, while **1a** exhibits strong fluorescence emission when excited at λ_{ex} = 380 nm, **2a** demonstrates markedly different behavior: it shows only weak emission in CH_3CN at its absorbance maximum (λ_{ex} = 510 nm), and undergoes near-complete fluorescence quenching under physiological conditions (PBS buffer, pH 7.4) (Figure S10). The cyclic voltammetry curves (Figure S11) also show distinct redox behavior: **2a** displays a reduction peak at −1.69 V vs. Ag/AgCl (assigned to the oxoisoaporphine ligand reduction), whereas **1a** shows no detectable reduction in this potential window. Taken together, these results provide support for the notion that **1a** and **2a** exhibit distinct physicochemical properties. To assess the effect of the bis-

https://doi.org/10.1021/jacs.5c00255
J. Am. Chem. Soc. 2025, 147, 15216−15228

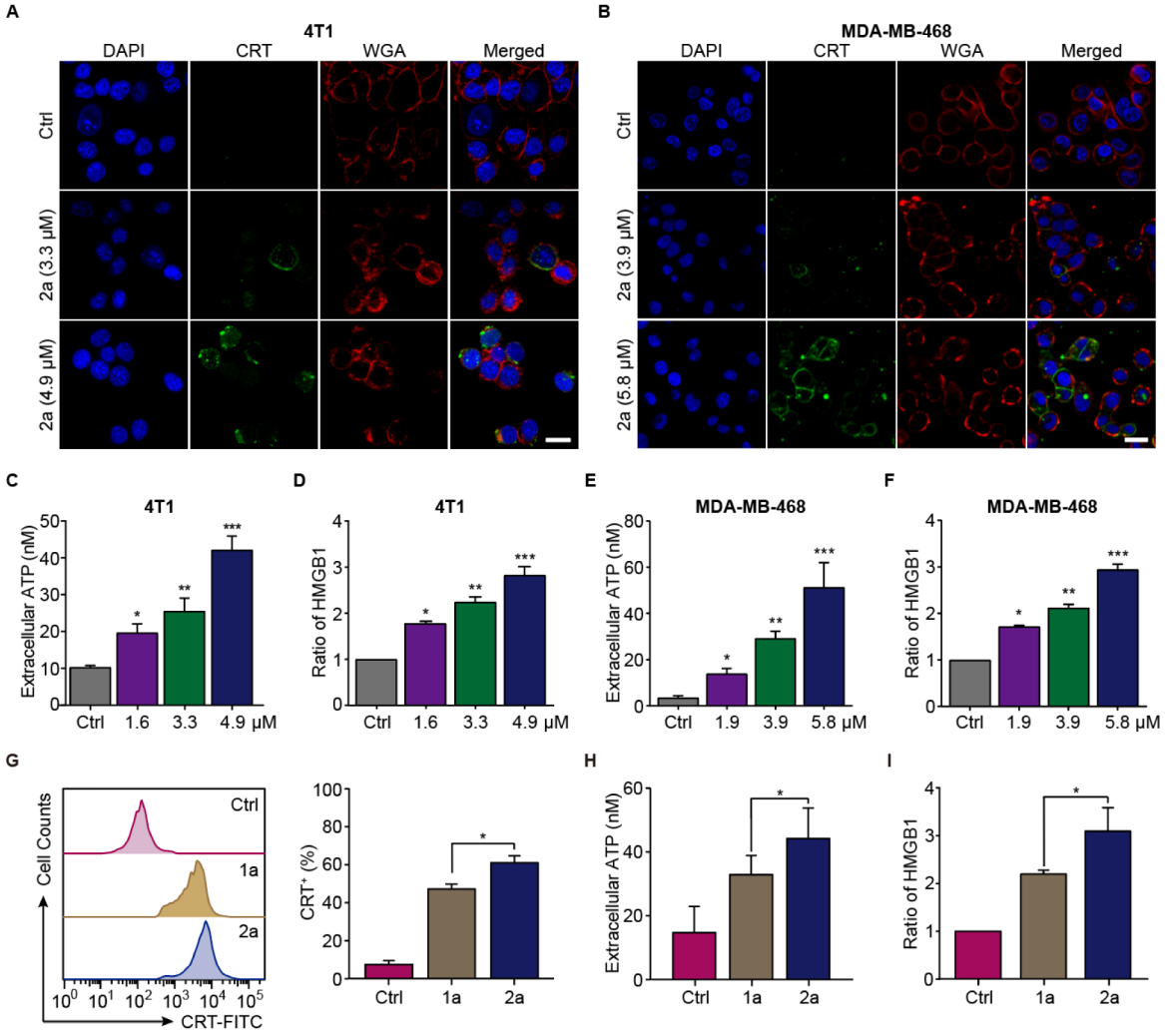

Figure 2. Induction of ICD-related DAMPs by **2a** in TNBC cells. (A, B) Representative confocal micrographs showing CRT translocation in 4T1 (A) and MDA-MB-468 (B) cells 12 h post-treatment with **2a**. Scale bars: 20 μm. (C, E) Levels of ATP release from 4T1 (C) and MDA-MB-468 (E) cells 6 h post-treatment with **2a**. (D, F) Ratio of released HMGB1 from 4T1 (D) and MDA-MB-468 (F) cells 12 h post-treatment with **2a**. (G) Flow cytometry analysis of CRT exposure in 4T1 cells 12 h post-treatment with **1a** (5 μM) and **2a** (5 μM). (H) Released ATP from 4T1 cells 6 h post-treatment with **1a** (5 μM) and **2a** (5 μM). (I) Ratio of released HMGB1 from 4T1 cells 12 h post-treatment with **1a** (5 μM) and **2a** (5 μM). Data represent mean ± SD (n = 3). *p < 0.05, **p < 0.01, ***p < 0.001, as compared with the control unless otherwise indicated.

NHC ligand L_b on the ICD activity of **2a**, three analogues, namely **Ir-NH$_2$**, **Ir-bpy**, and **Ir-phen** (Figure 1C), were prepared and characterized (Figures S12−S20).

In Vitro Cytotoxicity. Complexes **1a** and **2a** have similar coordination geometries but slightly different structures. Therefore, as an initial matter their anticancer activity was compared. Specifically, their cytotoxicity was tested in several triple-negative breast cancer (TNBC) cell lines (4T1, MDA-MB-231, MDA-MB-468, and BT549). As shown in Table S3, the oxoisoaporphine ligand L_a and the bis-NHC ligand L_b exhibited little cytotoxicity in these cell cultures. However, **2a** exhibited marked cytotoxicity against all tested TNBC lines, with IC_{50} values of 3.25−4.89 μM. These were slightly lower than those of **1a** (4.40−5.53 μM) and cisplatin (6.97−10.84 μM) used as a positive control. Additionally, the analogue **Ir-NH$_2$** displayed markedly lower cytotoxicity relative to **2a**, while **Ir-bpy** and **Ir-phen** exhibited comparable cytotoxicity to **2a** (Table S3). As **2a** displayed relatively better activity toward 4T1 and MDA-MB-468 cells, these two cell lines were selected for use in further mechanistic studies.

Investigation of ICD Activity. Based on the known ICD-inducing character of complex **1a** and the similar in vitro cytotoxicity of complexes **2a** and **1a** against TNBC cells, we assessed whether **2a** induces ICD-related DAMPs in TNBC cell lines. Surface exposure of CRT is a characteristic DAMP signal of ICD. To check whether this key marker was produced by **2a**, 4T1 cells were treated with **2a** and labeled with anti-CRT antibody. We found that **2a** enhanced the green immunofluorescence of CRT on the cell membrane surface and did so in a concentration-dependent manner (Figure 2A). The release of two other ICD-related DAMPs, ATP and HMGB1, in the supernatants of **2a**-treated 4T1 cells was also tested. The release of ATP increased in a concentration-dependent manner, reaching up to 42 nM in the cell culture medium after treatment with 5 μM of **2a** (Figure 2C). HMGB1 release followed a similar pattern (Figure 2D). In addition, the release of ATP and HMGB1 increased in a time-dependent manner (Figure S21). Next, we checked whether **2a** would produce these three characteristic DAMP signals in a separate cell line. MDA-MB-468 cells were used for these

https://doi.org/10.1021/jacs.5c00255
J. Am. Chem. Soc. 2025, 147, 15216−15228

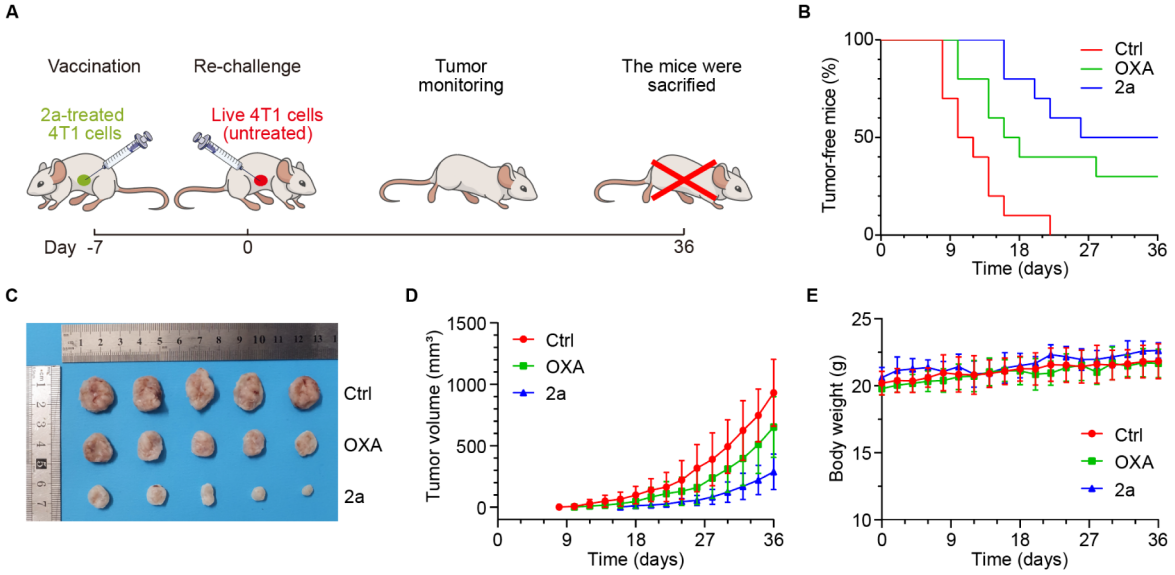

Figure 3. Anticancer studies in vivo. (A) Mouse tumor rechallenge assay (n = 10 per group) using the TNBC 4T1 cell line. (B) Percentage of tumor-free mice after rechallenging with fresh cancer cells seen for each treatment group (n = 10 per group). (C) Photograph of representative tumors removed from mice in each treatment group at the experimental end points. (D) Tumor volume changes for each treatment group (n = 10 per group). (E) Body weight evolution for tumor-free mice in each treatment group (n = 10 per group). OXA = oxaliplatin.

studies. As in 4T1 cells, CRT exposure (Figure 2B), ATP release (Figure 2E), and HMGB1 secretion (Figure 2F) were all increased in a concentration-dependent manner following treatment of MDA-MB-468 cells with **2a**. Taken in concert, these results led us to conclude that **2a** acts as an ICD inducer in TNBC cells.

To test whether the analogues **Ir-NH$_2$**, **Ir-bpy**, **Ir-phen**, and **1a** would likewise act as ICD inducers in vitro, their ability to promote the release of HMGB1 in 4T1 cells was studied under conditions identical to those above. Neither **Ir-NH$_2$**, **Ir-bpy**, nor **Ir-phen**, was found to alter significantly the released HMGB1 levels (Figure S22). Release was seen in the case of **1a**, but at a lower level than **2a** (Figure 2G–I), indicating that **2a** exhibited superior ICD activity to **1a**. These results prompted us to investigate the therapeutic effect of **2a** in vivo.

Vaccination Studies In Vivo. To evaluate whether **2a** could promote ICD-mediated tumor eradication in vivo, a vaccination experiment was conducted on syngeneic immunocompetent BALB/c mice (Figure 3A). OXA was used as a positive control. First, 2 × 10^6 4T1 cells were treated with **2a** (20 μM) or OXA (150 μM) for 6 h. Subsequently, the treated cells were injected (s.c.) into the left flank of mice (n = 10 per group). At day 0 (7 days after injection), the animals were reinjected with 1 × 10^4 4T1 fresh (i.e., untreated) cells in the right flank of mice. This low level of reinjection was chosen due to the rapid proliferation of 4T1 cells. Tumor development was then monitored daily. A mouse without any visible tumor in its right flank was designated as "tumor-free". On day 8 after the rechallenge, 30% of mice in the control group were found to have developed tumors. Meanwhile, OXA and **2a** delayed tumor development after the second inoculation (Figure 3B). In the OXA group, two mice carried tumors by day 10 (20%), while in the **2a** group, only by day 16 were two mice with tumors (20%) seen. On the 22nd day post-rechallenge, the percentage of tumor-free mice in the control group had dropped to zero, while it remained around 60% and 40% in the **2a** and OXA groups, respectively. In the OXA-treated mice, this percentage stabilized at 30% after 28 days. In contrast, 50% of the mice in the **2a**-treated group were stable and tumor-free after 26 days. Tumor growth was monitored up to 36 days with no further changes in the OXA and **2a** groups being noted (Figure 3C,D). On the 36th day after rechallenge the surviving animals were sacrificed. The tumors of the **2a** group were on average three times smaller than those of the control group and also noticeably smaller than those of the OXA group. Additionally, mice in all the three groups displayed similar and constant body weights throughout the experiment (Figure 3E).

To gain insights into the tumor progression disparities inferred from the in vivo immune responses noted above, high-dimensional profiling of several kinds of mouse tissues from each treatment group was conducted using cytometry by time of flight (CyTOF). The tested tissues included tumors, spleen, lymph nodes, and peripheral blood samples. Live immune cells were segregated via a series of gating steps using the CD45$^+$ marker antibody. Subsequently, a focused analysis was conducted on macrophages/monocytes, B cells, CD4$^+$ T cells, and CD8$^+$ T cells using classic markers (Table S4) from the identified live immune cell subsets. To present visually the different populations of immune cells across the control, OXA, and **2a** groups, two-dimensional t-stochastic neighbor embedding (tSNE) maps were generated (Figure 4A–D).

Activation of CD8$^+$ T cells in tumors is an established in vivo response to ICD.[53] The upregulation of CD38$^+$ and Ki67$^+$ expression serve as indicators of T cell activation and proliferation,[54,55] respectively. The **2a** and OXA groups displayed notably higher percentages of CD3$^+$CD8$^+$, CD3$^+$CD8$^+$CD38$^+$, and CD3$^+$CD8$^+$Ki67$^+$ T cells than the control group in the four tested tissues (Figure 4A–L). Moreover, in tumor tissues, the **2a** group had a higher percentage of these T cells than the OXA group (Figure 4E,I). These results are taken as evidence that treatment with **2a** activates CD3$^+$CD8$^+$ T cells. The expression levels of the cytokines granzyme B (GZMB), interferon γ (IFN-γ), and tumor necrosis factor α (TNF-α) were then quantified since these cytokines serve as indicators of the ability of CD8$^+$ T

https://doi.org/10.1021/jacs.5c00255
J. Am. Chem. Soc. 2025, 147, 15216–15228

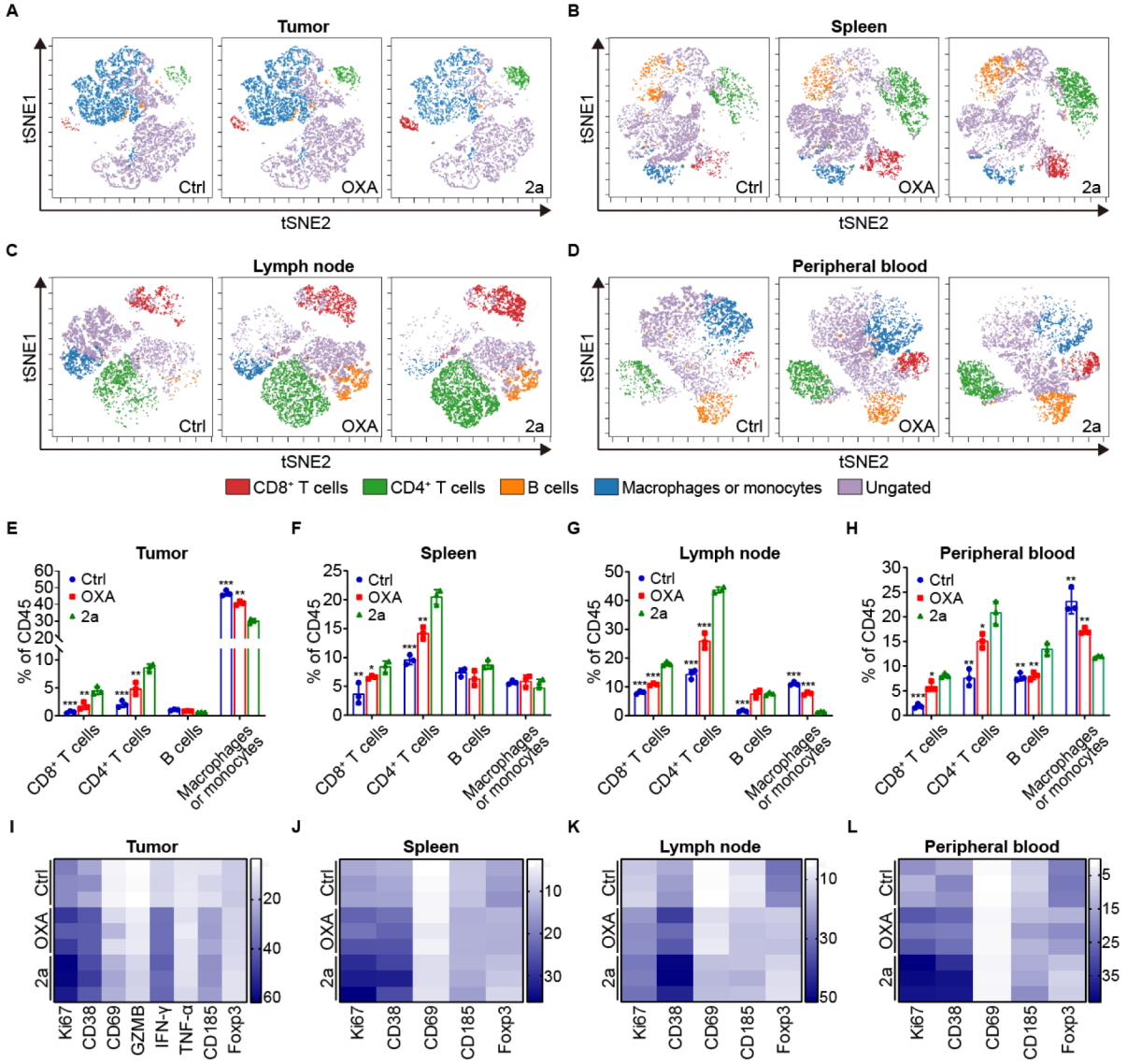

Figure 4. CyTOF analysis of immune cells in the rechallenge experiments. (A–D) Populations of several kinds of immune cells in tumors (A), spleen (B), lymph nodes (C), and peripheral blood samples (D) in each treatment group. (E–H) Percentage of immune cells based on the analyses in (A–D). Data represent mean ± SD ($n = 3$). *$p < 0.05$, **$p < 0.01$, ***$p < 0.001$, as compared with the **2a** group. (I–L) Heatmaps showing the proportion of immune cell subsets in tumors (I), spleen (J), lymph nodes (K), and peripheral blood samples (L).

cells to kill tumor cells.[56] In tumor tissues, the percentages of GZMB (13.45%), IFN-γ (38.31%), and TNF-α (10.92%) in $CD3^+CD8^+$ T cells were higher in the **2a** group than those in the control and OXA groups (Figures 4I and S23A).

Next, $CD69^+$ was used as a marker of tissue resident memory T cells (T_{RM}) allowing prolonged monitoring of tumor recurrence.[57] Compared to the control group, the **2a** group exhibited notably elevated proportions of $CD69^+$ expression within the $CD3^+CD8^+$ T cell subset in the lymph nodes, spleen, and tumors, while displaying slightly higher levels of these cells than the OXA group (Figure 4I–K). These results support the suggestion that **2a**-induced ICD in cancer cells triggers an anticancer immune response and that this effect is greater than that elicited by OXA.

$CD4^+$ T cells are also important in modulating the immune response within the tumor site.[58] Compared to the control group, both the **2a** and OXA groups exhibited elevated proportions of total $CD3^+CD4^+$ T cells and T_h cells ($CD3^+CD4^+CD185^+$), with the **2a** group further demonstrating a slight increase over the OXA group (Figure 4E,I). All tissues in the **2a** group displayed a reduced proportion of T_{reg} cells ($CD3^+CD4^+Foxp3^+$ T cells), compared to those in the control and OXA groups (Figures 4I–L). T_{reg} cells are known to suppress cytotoxic T cell activity by secreting immunosuppressive cytokines.[59] Specifically, the proportion of T_{reg} cells in tumor tissues was 15.63% in the control group, 10.81% in the **2a** group, and 13.22% in the OXA group (Figures 4I and S23B). Overall, these results support the suggestion that injection of **2a**-treated cells results in a pronounced suppression of T_{reg} cells, thereby promoting an immune response which surpasses that exhibited by OXA.

In Vivo Therapeutic Efficacy of 2a Synergistically with Anti-PD1. To test whether the proposed anticancer immune-activating mechanism of **2a** would translate into a benefit in vivo, its therapeutic potential was assessed in murine models. First, KM mice were used to assess the safety of **2a** at doses of 10, 20, and 30 mg/kg, administered intravenously through the retro-orbital venous sinus once every 2 days.

https://doi.org/10.1021/jacs.5c00255
J. Am. Chem. Soc. 2025, 147, 15216–15228

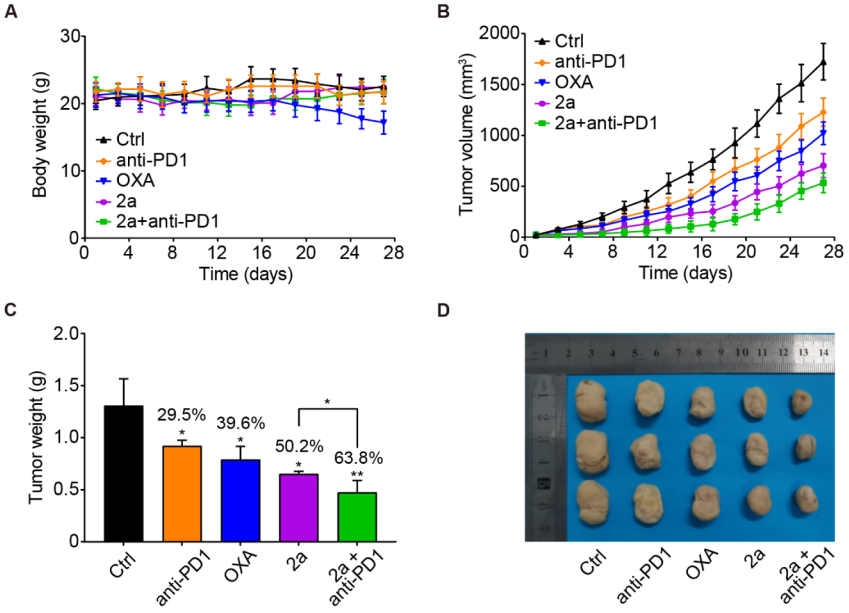

Figure 5. In vivo anticancer experiments. (A) Tumor volumes of 4T1 xenograft mice (n = 5 per group) in the indicated treatment groups. (B) Body weights of mice bearing 4T1 cells (n = 5 per group) in each treatment group. (C) Weights of tumors in each treatment group at the experimental end point. The percentage indicated above each bar represents the inhibition rate of tumor growth (IRT) value for each group. (D) Photograph of representative tumors in each treatment group.

Although all mice survived, treatment with 30 mg/kg of **2a** caused significant lowering of the body weight relative to control (Figure S24). Therefore, 20 mg/kg was chosen for further experiments.

Using this dose, the in vivo therapeutic potential of **2a** in BALB/c mice bearing 4T1 xenograft tumors was evaluated. As some chemotherapeutic drugs serving as ICD inducers can synergistically amplify the therapeutic effects of PD-1/PD-L1 blockade agents,[8−10] we tested the therapeutic effects of **2a** with a PD-1 inhibitor (anti-mouse PD1 (CD279) (BioXcell, #BP0146). When the 4T1 tumor volume of the BALB/c mice reached about ∼20 mm^3 (day 0), the animals were treated intravenously through the retro-orbital venous sinus with OXA (7 mg/kg), anti-PD1 (200 μg/mouse), **2a** (20 mg/kg), or a combination of **2a** (20 mg/kg) and anti-PD1 (200 μg/mouse) once every 2 days. The selection of doses and administration frequencies was decided according to both the safety of the compounds and the well-being of the mice. The dose of OXA selected for this study was based on typical dosing used in in vivo antitumor studies. Unlike the OXA-treated group, which underwent a slight body weight decrease, treatment with **2a** and/or anti-PD1 did not induce a significant weight loss (Figure 5A). These results provide support for the notion that **2a** is safe at the administered dose. Compared with the vehicle, **2a** inhibited tumor growth in a statistically significant manner and performed better than OXA and anti-PD1 (Figure 5B). Moreover, although the effect is modest, **2a** and anti-PD1 displayed an apparent synergistic antitumor effect (Figure 5B).

At the end of the experiment, we removed and measured the mass of the tumors, in order to determine the inhibition rate of tumor growth (IRT). Notably, complex **2a** demonstrated an IRT of 50.2%, exceeding the 39.6% achieved by OXA and the 29.5% achieved by anti-PD1 (Figure 5C). Notably, the combination therapy produced the highest IRT (63.8%) (Figure 5C). The tumor volume measurements confirm this result (Figure 5D). Altogether, these findings further support the proposition that **2a** shows promise as chemoimmunotherapeutic agent that can be used to enhance the anti-tumor effects of PD1 therapies. These results prompted us to investigate the underlying mechanism of ICD induction triggered by **2a**.

Target Profiling. Our previous study identified that complex **1a** induced ICD through BiP, which was destabilized at around 60 °C.[33] To assess whether complex **2a** also targeted BiP, the cellular thermal shift and isothermal dose−response assays (CETSA and ITDR, respectively) were carried out. In 4T1 cells, the CETSA results revealed that **2a** did not appreciably affect the thermal stability of BiP across the 54−64 °C temperature range (Figure 6A). Furthermore, treatment with any concentration of **2a** at 60 °C did not markedly impact the amount of BiP in the soluble fraction in the ITDR assay (Figure 6B). On the basis of these results, we conclude that **2a** induces ICD by targeting proteins other than BiP. We thus sought to determine the major target of **2a**.

With this goal in mind, a thermal proteome profiling (TPP) experiment was carried out as described previously (Scheme S3).[60,61] In this CETSA-based method, a significant change in the melting temperature (T_m) of a protein upon ligand exposure generally serves as evidence of protein−ligand binding. Combined with MS-based quantitative proteomics, this approach allows the identification of the proteins targeted by specific compounds.

For this analysis, 4T1 cell proteins were extracted by means of freeze−thaw cycles. The extracts were then treated with **2a** and heated to temperatures between 37 and 67 °C to denature the various proteins. Tryptic peptides were individually labeled with iTRAQ 8-plex isobaric tags and analyzed quantitatively. Melting curves and T_m values for the proteins were generated using the TPP R analysis package. Table S5 lists the possible target proteins, the thermal stability of which was increased or decreased, including cathepsin D (Cat D/CTSD), peroxiredoxin-1 (PRDX1), DNA replication licensing factor MCM5 (MCM5), and coatomer subunit gamma-1 (COPG1). For PRDX1, MCM5, and COPG1, the CETSA results showed no

https://doi.org/10.1021/jacs.5c00255
J. Am. Chem. Soc. 2025, 147, 15216−15228

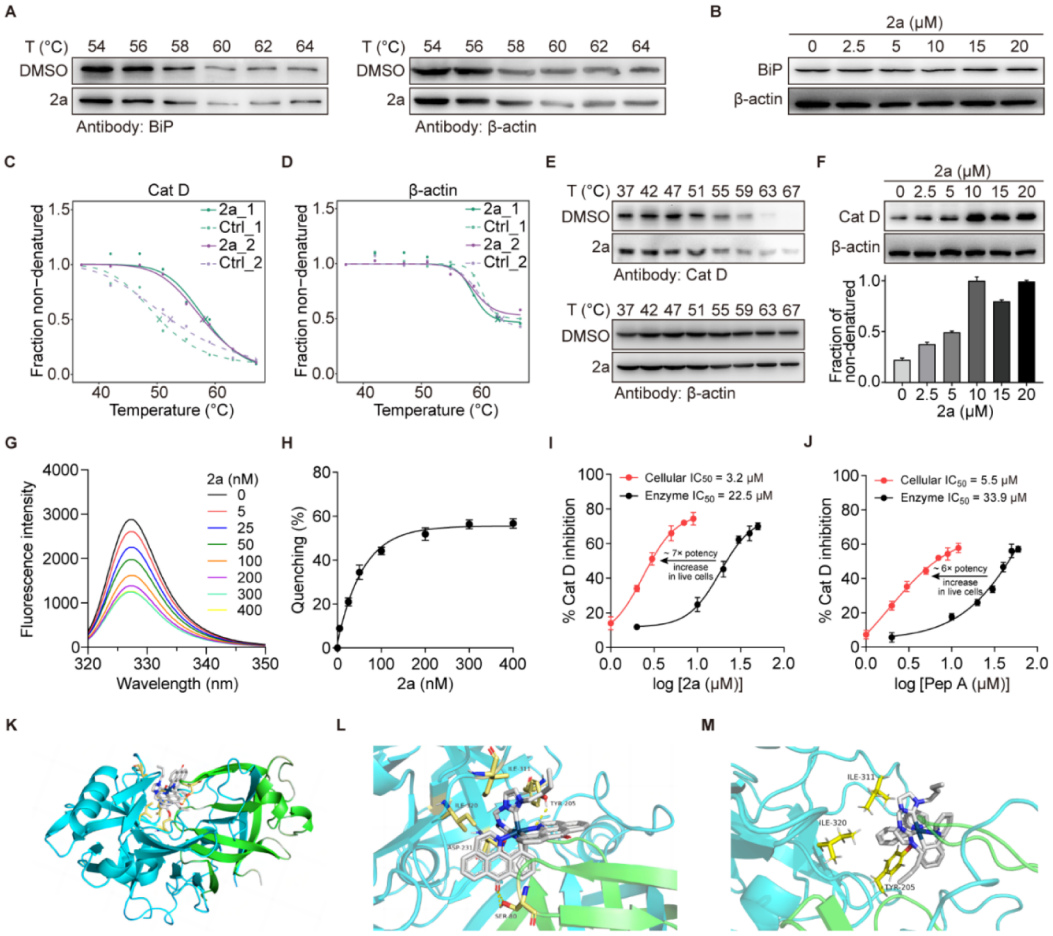

Figure 6. Studies of the interaction between **2a** and Cat D. (A) Immunoblots from CETSA (3.3 μM of **2a**) with BiP and β-actin antibodies. (B) Immunoblots from ITDR assays (60 °C) with BiP antibody. (C, D) Melting curves of Cat D (C) and β-actin (D) recorded in the absence and presence of **2a** (3.3 μM), as determined by thermal proteome profiling (TPP). **2a**_1, **2a**_2, Ctrl_1, and Ctrl_2 represent two independent replicates under the same conditions for the **2a** and control groups, respectively. (E) Immunoblots from CETSA (3.3 μM in **2a**) with Cat D or β-actin antibodies. (F) Immunoblots from ITDR assays (63 °C) with Cat D antibody. (G) Fluorescence emission spectra of Cat D (10 nM) recorded upon the addition of **2a**. (H) Fluorescence quenching curve for Cat D (10 nM) seen upon the addition of **2a**. (I, J) Inhibition of Cat D activity determined after the addition of **2a** (I) or pep A (J) at the indicated concentrations. Data represent quantification of cellular Cat D inhibition (red) compared with inhibition of the purified protein (black). (K) The highest-scoring molecular docking conformation corresponding to the binding of **2a** with Cat D. (L, M) Predicted interaction modes for **2a** (L) and **1a** (M), and Cat D. The amino acid residues involved in the binding interactions are labeled. H-bonds appear as yellow dashed lines. Data represent mean ± SD (n = 3).

clear **2a**-induced thermal stability changes, leading us to conclude that these proteins are not targets of **2a**. Meanwhile, both the thermal proteome analysis and CETSA experiments revealed that **2a** increased the thermal stability of Cat D (Figure 6C–E) with an increase of about 7 °C in the T_m being observed ($p < 0.05$) (Figure 6C). In addition, the CETSA results revealed a difference in the thermal stability of Cat D in the presence or absence of **2a** at about 63 °C (Figure 6E). The ITDR assay also revealed a dose-dependent thermal stabilization of Cat D by **2a** (Figure 6F). Altogether, these results lead us to conclude that **2a** binds to Cat D and stabilizes it.

The binding affinity of **2a** to Cat D was quantified through a fluorescence quenching experiment. Ligands that quench the intrinsic tryptophan (Trp) fluorescence of a protein upon binding allow the dissociation constant (K_D) to be calculated from the fluorescence quenching curves with lower K_D values indicating a relatively higher ligand-protein association. Therefore, the Trp fluorescence (λ_{ex}: 295 nm; λ_{em}: 328 nm) was monitored. As expected, **2a** was found to quench the Trp fluorescence of Cat D in a concentration-dependent manner (Figure 6G,H). The K_D value of **2a** was calculated to be 2.7 μM. Pepstatin A (pep A) and myricitrin, both known inhibitors of Cat D,[62,63] exhibited K_D values of 3.4 μM (Figure S25) and 4.3 μM (Figure S26), respectively, which are slightly higher than that of **2a**. Notably, neither **1a** nor ligand L_a showed considerable quenching of the Trp fluorescence of Cat D (Figure S27), supporting the specificity of the interaction between **2a** and Cat D. Further evidence was provided by circular dichroism (CD) spectroscopy. Upon incubation with **2a**, the CD spectrum of Cat D exhibited a pronounced shift in the negative band at 213 nm to 225 nm (Figure S28). This shift indicates a subtle change in the secondary structure of Cat D upon binding to **2a**. In contrast, neither **1a** nor ligand L_a induced such changes. To gain insight into the binding mode, molecular docking studies of **2a** with Cat D (PDB ID: 6QCB) were performed as shown in Figure 6, panels K and L. The structure with the highest score provides support for the suggestion that **2a** is associated within the active pocket domain of Cat D with SER80, TYR205, ILE311, ILE320, and ASP231 interacting directly with **2a**, presumably disturbing the

https://doi.org/10.1021/jacs.5c00255
J. Am. Chem. Soc. 2025, 147, 15216–15228

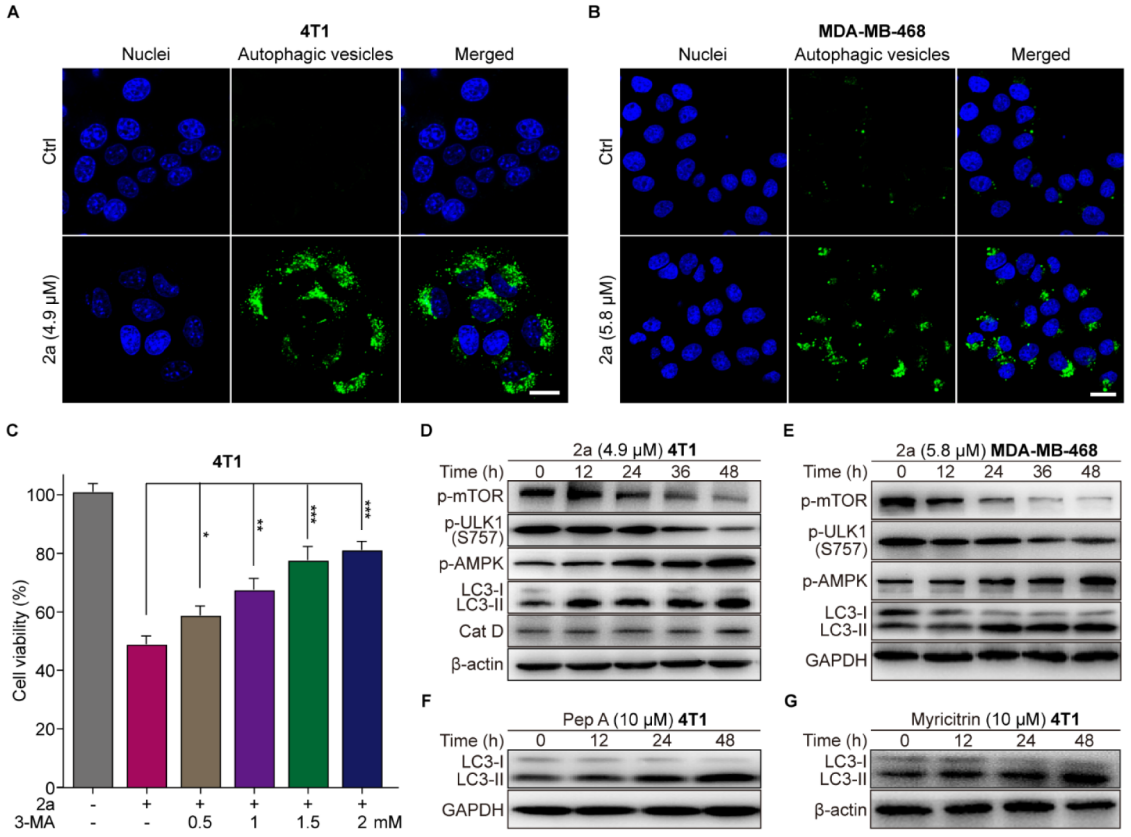

Figure 7. Autophagy in TNBC cells induced by **2a**. (A, B) Confocal images presenting autophagic vesicles in 4T1 (A) and MDA-MB-468 (B) cells after incubation with **2a** for 24 h. The nuclei were stained with DAPI (blue). Scale bars: 20 μm. (C) Viability of 4T1 cells co-treated with 3-MA and **2a** (3.3 μM) for 48 h. Data represent mean ± SD (n = 3). *p < 0.05, **p < 0.01, ***p < 0.001, as compared with the indicated group. (D, E) Western blot analyses of autophagy-related proteins after incubation of 4T1 (D) and MDA-MB-468 (E) cells with **2a** for 0−48 h. (F, G) Western blot analysis of LC3 after incubation of 4T1 cells with pep A (F) and myricitrin (G) for 0−48 h.

function of Cat D. Non-covalent electrostatic interactions appear to constitute the main driver of the inferred Cat D-**2a** binding. This is not unreasonable since the cavity is electronegatively polarized (Figure S29) while **2a** is positively charged. Hydrogen bonds are also formed between the carbonyl group of **2a** and SER80, and between the quinoline nitrogen atom and TYR205. Complex **1a** binds only weakly to the active pocket of Cat D, with a calculated binding energy of −3.93 kcal/mol, which is higher than that of **2a** (−8.62 kcal/mol). Furthermore, no hydrogen bonding interactions were observed between **1a** and Cat D (Figure 6M). These results are taken as evidence that **1a** does not form a stable complex with Cat D.

To confirm further that a compound can target a specific protein, fluorescence colocalization or other methods are generally used to verify that the compound in question can be enriched in specific subcellular organelles. Given that **2a** does not exhibit fluorescence (Figure S10), we analyzed its subcellular distribution in 4T1 cells using ICP−MS. The results revealed that **2a** predominantly accumulates in lysosomes after 24 h incubation (Figure S30). These results further support the notion that **2a** targets Cat D, because Cat D is primarily localized in lysosomes.

The effect of **2a** on the aspartic protease activity of Cat D was also assessed both in 4T1 cells and in purified form. As expected, **2a** inhibited the activity of Cat D and demonstrated greater potency than pep A in both contexts (Figure 6I,J). Specifically, **2a** concentration-dependently inhibited the activity of Cat D with an IC_{50} value of 3.2 μM in cellular assays, which was approximately 7-fold lower than the IC_{50} value obtained using purified Cat D (22.5 μM). This discrepancy is consistent with a previous report[64] and highlights that IC_{50} values for enzyme inhibition are dependent on the experimental conditions. For instance, the enzyme concentration in cell-free assays is typically much higher than in cellular assays, which may account for the observed difference. Altogether, these results are taken as evidence that **2a** binds to the active domain of Cat D and inhibits its activity.

Induction of Autophagy by Cat D Inhibition. Cat D inhibition can induce autophagy.[62] Thus, we postulated that **2a** could induce autophagy. To confirm this, autophagy was assessed with a green fluorescent dye which marks autophagic vesicles selectively. As shown in Figure 7A, the generation of autophagic vesicles in 4T1 cells significantly increased after incubation with **2a** for 24 h, as would be expected were autophagy occurring. Meanwhile, pretreatment with 3-MA (an inhibitor of autophagy) increased the viability of **2a**-treated cells in a dose-dependent manner (Figure 7C). Notably, pretreating cells with 2 mM 3-MA decreased cell death by ∼29%, leading us to conclude that autophagy constitutes the main cell death mode induced by **2a**. Autophagy induction through Cat D inhibition is reportedly regulated by the LKB1-AMPK-ULK1 signaling axis.[62] To evaluate whether **2a** could induce autophagy through this axis, the expression levels of the axis-related proteins were examined in 4T1 cells treated with

https://doi.org/10.1021/jacs.5c00255
J. Am. Chem. Soc. 2025, 147, 15216−15228

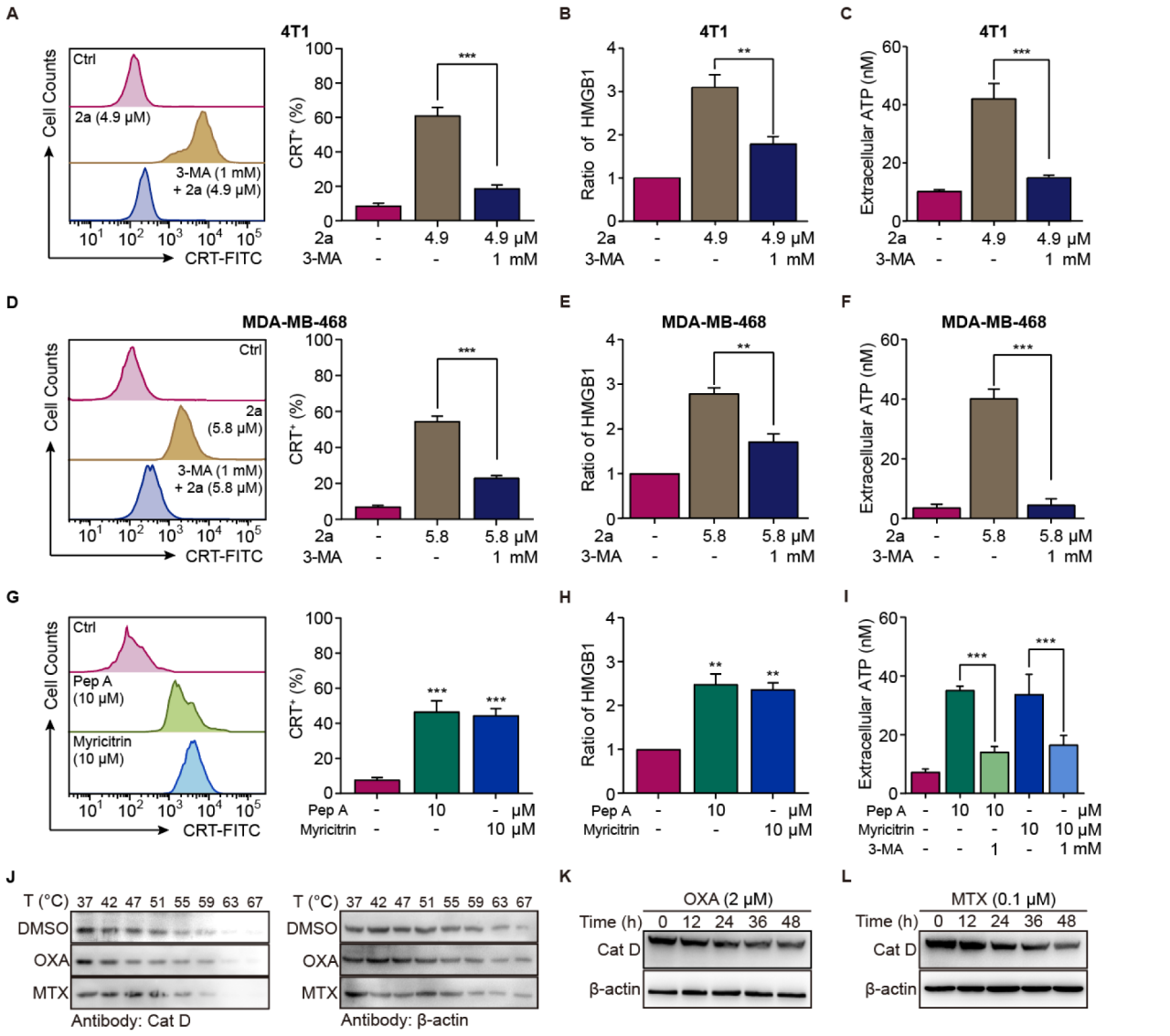

Figure 8. Induction of autophagy-dependent ICD in TNBC cells. (A, D) Flow cytometry analyses of CRT exposure in 4T1 (A) and MDA-MB-468 (D) cells 12 h post-treatment with **2a** and 3-MA. (B, E) Ratio of released HMGB1 in 4T1 (B) and MDA-MB-468 (E) cells 12 h post-treatment with **2a** and 3-MA. (C, F) ATP released from 4T1 (C) and MDA-MB-468 (F) cells 6 h post-treatment with **2a** and 3-MA. (G) Flow cytometric analysis of CRT exposure in 4T1 cells 12 h after treating with pep A and myricitrin. (H) Ratio of released HMGB1 from 4T1 cells 12 h post-treatment with pep A and myricitrin. (I) ATP released from 4T1 cells 6 h post-treatment with pep A and myricitrin. (J) Immunoblots from CETSA (2 μM of OXA and 0.1 μM of mitoxantrone (MTX)) with Cat D or β-actin antibodies. (K, L) Expression level of Cat D in response to OXA (K) and MTX (L). Data represent mean ± SD (n = 3). *p < 0.05, **p < 0.01, ***p < 0.001, as compared with the control unless otherwise indicated.

2a. As expected, **2a** downregulated the expression levels of p-mTOR and p-ULK1 (S757) and an upregulation of p-AMPK in a time-dependent manner were seen, although it did not affect the levels of Cat D (Figure 7D). The levels of LC3-II, a general biomarker of autophagy, also increased in a time-dependent manner (Figure 7D). However, the level of LC3-II was not affected by **1a** treatment (Figure S31), leading us to conclude that **1a** does not induce autophagy. We thus suggest that **1a** and **2a** have different mechanisms of action.

Similar to what was seen in in 4T1 cells, treatment with **2a** increased the generation of autophagic vesicles in MDA-MB-468 cells (Figure 7B), while affecting the expression of LKB1-AMPK-ULK1 signaling axis-related proteins (Figure 7E). In addition, pep A and myricitrin, which both can inhibit Cat D, were also upregulated to the level of LC3-II and in a time-dependent manner in 4T1 cells (Figure 7F,G). Considered in concert, these results provide support for the conclusion that **2a** can induce autophagy and does so by inhibiting Cat D in TNBC cells.

Induction of Autophagy-Dependent ICD by Cat D Inhibition. Since both autophagy and ICD induction are required for the secretion of ATP,[65,66] and these processes can be induced by **2a** simultaneously, we postulated that the ICD effects produced by **2a** were autophagy-dependent. To confirm or refute this supposition, the effects of 3-MA pretreatment on **2a**-induced DAMP signals were investigated. As expected, 3-MA pretreatment reduced the extent of **2a**-induced CRT exposure, ATP release, and HMGB1 secretion in both 4T1 (Figure 8A−C) and MDA-MB-468 cells and did so in a statistically significant manner (Figure 8D−F). We thus conclude that **2a**-induced ICD is dependent on autophagy in TNBC cells.

https://doi.org/10.1021/jacs.5c00255
J. Am. Chem. Soc. 2025, 147, 15216−15228

To confirm that Cat D inhibition caused autophagy-dependent ICD, the ICD-inducing activity of the Cat D inhibitors pep A and myricitrin were assessed, respectively. As shown in Figure 8G−I, CRT exposure, ATP release, and HMGB1 secretion were all increased by both pep A and myricitrin in 4T1 cells, leading us to suggest their potential in eliciting ICD. As anticipated, 3-MA inhibited the ATP release induced by pep A and myricitrin (Figure 8I). Altogether, these results support the conclusion that inhibiting Cat D activity induces autophagy-dependent ICD in TNBC cells.

Cat D Engagement by Other Autophagy-Dependent ICD Agents. To document the general role of Cat D in autophagy-dependent ICD induction, the autophagy-dependent ICD agents OXA and MTX[67] were investigated. CETSA analyses revealed that OXA and MTX did not notably affect the thermal stability of Cat D in 4T1 cells across the 37−67 °C temperature range (Figure 8J), supporting the inference that OXA and MTX do not bind to Cat D. Subsequently, the expression level of Cat D was quantified in 4T1 cells treated with OXA and MTX. Both agents downregulated the expression level of Cat D in a time-dependent manner (Figure 8K,L), a finding that may reflect interference with genomic DNA transcription.[68] Independent of mechanism, Cat D downregulation by these agents may play a role in eliciting autophagy-dependent ICD. We thus posit that Cat D will emerge as a promising target for inducing autophagy-dependent ICD effects.

CONCLUSIONS

In summary, we developed a new cyclometalated Ir(III) complex, **2a**, incorporating an oxoisoaporphine moiety and a bis-NHC ligand. As judged by ICD-induced DAMPs complex **2a** induces greater ICD activity than its previously reported analogue **1a** (bearing phenylpyridine ligands) against TNBC cells. A TPP experiment revealed that this ICD inducer targeted Cat D, not BiP. Further biochemical studies and molecular docking revealed that **2a** effectively bound to and stabilized Cat D, inhibiting its aspartic protease activity more effectively than pep A (a reported Cat D inhibitor). Mechanistically, **2a** induces autophagy-dependent ICD through the LKB1-AMPK-ULK1 signaling axis by inhibiting Cat D activity. Preliminary experiments with other autophagy-dependent ICD inducers demonstrate the potential generality of Cat D inhibition as a determinant of action. The identification of Cat D as a target and the effectiveness of complex **2a** may guide future ICD agent design. We suggest that metal complexes will play a key role in this effort since they can be systematically regulated by ligand design to interact with particular biomolecular targets;[69] however, other small molecules that inhibit Cat D (by blocking either its expression or activity) likewise warrant study. Efforts to discover new ICD inducers in the context of this paradigm are currently underway in our laboratories.

Finally, our work highlights an iridium(III) compound that is able to induce ICD in a mechanism that is believed to be different from other Ir(III) ICD agents. At the very least, it provides a complement to approaches being pursued by others. More broadly, there is a desperate need for new anticancer approaches. For instance, there are only two FDA-approved chemotherapeutic regimens for pancreatic cancer. Moreover, pancreatic cancer is refractory to FDA-approved immunooncology agents. ICD offers the promise of jump-starting the anticancer immune system and could be transformative for patients. There is a very long way to go, but the hope is that showing how a small modification in the backbone of an iridium complex can cause a change in ICD induction determinants from a traditional ER stress through BiP mechanism to one involving Cat D will help advance the field.

ASSOCIATED CONTENT

Supporting Information

The Supporting Information is available free of charge at https://pubs.acs.org/doi/10.1021/jacs.5c00255.

Materials and instruments, synthesis steps, and experimental procedures; ESI−MS spectra, NMR spectra, and HPLC chromatograph; UV−vis absorption spectra, emission spectra, and cyclic voltammetry curves; time-dependently induction of ATP and HMGB1 release; release of HMGB1 from 4T1 cells treated with Ir analogues; percentage of immune cells in $CD3^+CD8^+$ and $CD3^+CD4^+$ T cells in tumor tissues; dose screening of **2a** for in vivo mouse experiment; fluorescence emission spectra and fluorescence quenching curves; far-UV circular dichroism spectra; predicted interaction between **2a** and Cat D by molecular docking; uptake of **2a** by 4T1 cells; western blots of LC3 after incubating 4T1 cells with **1a**; iridium complexes showing ICD activity; IC_{50} values of Ir(III) complexes, cisplatin and ligands; marker panel for CyTOF; and proteins with changes of thermal stability under the treatment of **2a** (PDF)

Accession Codes

Deposition Number 2333613 contains the supplementary crystallographic data for this paper. These data can be obtained free of charge via the joint Cambridge Crystallographic Data Centre (CCDC) and Fachinformationszentrum Karlsruhe Access Structures service.

AUTHOR INFORMATION

Corresponding Authors

Taotao Zou − *Guangdong Key Laboratory of Chiral Molecule and Drug Discovery, School of Pharmaceutical Science, Sun Yat-Sen University, Guangzhou 510006, China;* orcid.org/0000-0001-9129-4398; Email: zoutt3@mail.sysu.edu.cn

Jonathan L. Sessler − *Department of Chemistry, The University of Texas at Austin, Austin, Texas 78712-1224, United States;* orcid.org/0000-0002-9576-1325; Email: sessler@cm.utexas.edu

Hong Liang − *Key Laboratory for Chemistry and Molecular Engineering of Medicinal Resources (Ministry of Education of China), Guangxi Key Laboratory of Chemistry and Molecular Engineering of Medicinal Resources, School of Chemistry and Pharmaceutical Sciences, Guangxi Normal University, Guilin 541004, China*; Email: hliang@gxnu.edu.cn

Ke-Bin Huang − *Key Laboratory for Chemistry and Molecular Engineering of Medicinal Resources (Ministry of Education of China), Guangxi Key Laboratory of Chemistry and Molecular Engineering of Medicinal Resources, School of Chemistry and Pharmaceutical Sciences, Guangxi Normal University, Guilin 541004, China;* orcid.org/0000-0003-4773-4442; Email: kbhuang@mailbox.gxnu.edu.cn

Authors

Yuan Lu − *Key Laboratory for Chemistry and Molecular Engineering of Medicinal Resources (Ministry of Education of China), Guangxi Key Laboratory of Chemistry and Molecular Engineering of Medicinal Resources, School of Chemistry and Pharmaceutical Sciences, Guangxi Normal University, Guilin 541004, China; Guangxi College Key Laboratory of Innovation Research on Medical and Engineering Integration & Liuzhou Key Laboratory of Guizhong Characteristic Medicinal Resources Development, School of Medicine, Guangxi University of Science and Technology, Liuzhou 545005, China*

Feng-Yang Wang − *Key Laboratory for Chemistry and Molecular Engineering of Medicinal Resources (Ministry of Education of China), Guangxi Key Laboratory of Chemistry and Molecular Engineering of Medicinal Resources, School of Chemistry and Pharmaceutical Sciences, Guangxi Normal University, Guilin 541004, China; Key Laboratory of Medical Biotechnology and Translational Medicine, Education Department of Guangxi Zhuang Autonomous Region, School of Intelligent Medicine and Biotechnology, Guilin Medical University, Guilin 541004, China*

Matthew S. Levine − *Department of Chemistry, The University of Texas at Austin, Austin, Texas 78712-1224, United States;* orcid.org/0000-0002-2622-2678

Hai-Rong Shi − *Key Laboratory for Chemistry and Molecular Engineering of Medicinal Resources (Ministry of Education of China), Guangxi Key Laboratory of Chemistry and Molecular Engineering of Medicinal Resources, School of Chemistry and Pharmaceutical Sciences, Guangxi Normal University, Guilin 541004, China*

Yuan Wang − *Guangdong Key Laboratory of Chiral Molecule and Drug Discovery, School of Pharmaceutical Science, Sun Yat-Sen University, Guangzhou 510006, China*

Xiaolin Xiong − *Guangdong Key Laboratory of Chiral Molecule and Drug Discovery, School of Pharmaceutical Science, Sun Yat-Sen University, Guangzhou 510006, China*

Liang-Mei Yang − *Key Laboratory for Chemistry and Molecular Engineering of Medicinal Resources (Ministry of Education of China), Guangxi Key Laboratory of Chemistry and Molecular Engineering of Medicinal Resources, School of Chemistry and Pharmaceutical Sciences, Guangxi Normal University, Guilin 541004, China*

Ya-Qian Shi − *Key Laboratory for Chemistry and Molecular Engineering of Medicinal Resources (Ministry of Education of China), Guangxi Key Laboratory of Chemistry and Molecular Engineering of Medicinal Resources, School of Chemistry and Pharmaceutical Sciences, Guangxi Normal University, Guilin 541004, China;* orcid.org/0000-0003-3549-6037

Complete contact information is available at: https://pubs.acs.org/10.1021/jacs.5c00255

Author Contributions

#Y.L., F.-Y.W., and M.S.L. contributed equally to this work.

Notes

The authors declare no competing financial interest.

■ ACKNOWLEDGMENTS

This work was supported in part by the Foundation of Guangxi Science and Technology Program (Grant No. AD22035193 to F.-Y.W. and AD25069021 to K.-B.H.) and the National Natural Science Foundation of China (Grant No. 22267005 to F.-Y.W. and 22177022 to H.L.). The work in Austin was supported by the National Institutes of Science (CA 068682 to J.L.S.) and the Robert A. Welch Foundation (F-0018 to J.L.S.). The work in SYSU was supported by Guangdong Basic and Applied Basic Research Foundation (No. 2024B1515040028). This work was also supported in part by the Central Guidance for Local Science and Technology Development Program (No. ZY20230103).

■ REFERENCES

(1) Galluzzi, L.; Vitale, I.; Warren, S.; Adjemian, S.; Agostinis, P.; Martinez, A. B.; Chan, T. A.; Coukos, G.; Demaria, S.; Deutsch, E.; Draganov, D.; Edelson, R. L.; Formenti, S. C.; Fucikova, J.; Gabriele, L.; Gaipl, U. S.; Gameiro, S. R.; Garg, A. D.; Golden, E.; Han, J.; Harrington, K. J.; Hemminki, A.; Hodge, J. W.; Hossain, D. M. S.; Illidge, T.; Karin, M.; Kaufman, H. L.; Kepp, O.; Kroemer, G.; Lasarte, J. J.; Loi, S.; Lotze, M. T.; Manic, G.; Merghoub, T.; Melcher, A. A.; Mossman, K. L.; Prosper, F.; Rekdal, Ø.; Rescigno, M.; Riganti, C.; Sistigu, A.; Smyth, M. J.; Spisek, R.; Stagg, J.; Strauss, B. E.; Tang, D.; Tatsuno, K.; van Gool, S. W.; Vandenabeele, P.; Yamazaki, T.; Zamarin, D.; Zitvogel, L.; Cesano, A.; Marincola, F. M. Consensus Guidelines for the Definition, Detection and Interpretation of Immunogenic Cell Death. *J. Immunother. Cancer* **2020**, *8* (1), No. e000337.

(2) Zhang, L.; Montesdeoca, N.; Karges, J.; Xiao, H. Immunogenic Cell Death Inducing Metal Complexes for Cancer Therapy. *Angew. Chem. Int. Ed.* **2023**, *62* (21), No. e202300662.

(3) Sen, S.; Won, M.; Levine, M. S.; Noh, Y.; Sedgwick, A. C.; Kim, J. S.; Sessler, J. L.; Arambula, J. F. Metal-Based Anticancer Agents as Immunogenic Cell Death Inducers: The Past, Present, and Future. *Chem. Soc. Rev.* **2022**, *51* (4), 1212−1233.

(4) Galluzzi, L.; Guilbaud, E.; Schmidt, D.; Kroemer, G.; Marincola, F. M. Targeting Immunogenic Cell Stress and Death for Cancer Therapy. *Nat. Rev. Drug Discovery* **2024**, *23* (6), 445−460.

(5) Kar, A.; Jain, D.; Kumar, S.; Rajput, K.; Pal, S.; Rana, K.; Kar, R.; Jha, S. K.; Medatwal, N.; Yavvari, P. S.; et al. A Localized Hydrogel-Mediated Chemotherapy Causes Immunogenic Cell Death Via Activation of Ceramide-Mediated Unfolded Protein Response. *Sci. Adv.* **2023**, *9* (26), No. eadf2746.

(6) Srivastava, S.; Furlan, S. N.; Jaeger-Ruckstuhl, C. A.; Sarvothama, M.; Berger, C.; Smythe, K. S.; Garrison, S. M.; Specht, J. M.; Lee, S. M.; Amezquita, R. A.; Voillet, V.; Muhunthan, V.; Yechan-Gunja, S.; Pillai, S. P. S.; Rader, C.; Houghton, A. M.; Pierce, R. H.; Gottardo, R.; Maloney, D. G.; Riddell, S. R. Immunogenic Chemotherapy Enhances Recruitment of CAR-T Cells to Lung Tumors and Improves Antitumor Efficacy When Combined with Checkpoint Blockade. *Cancer Cell.* **2021**, *39* (2), 193−208.

(7) Zhou, Z.; Mai, Y.; Zhang, G.; Wang, Y.; Sun, P.; Jing, Z.; Li, Z.; Xu, Y.; Han, B.; Liu, J. Emerging Role of Immunogenic Cell Death in Cancer Immunotherapy: Advancing Next-Generation Car-T Cell Immunotherapy by Combination. *Cancer Lett.* **2024**, *598*, 217079.

(8) Limagne, E.; Thibaudin, M.; Nuttin, L.; Spill, A.; Derangère, V.; Fumet, J.-D.; Amellal, N.; Peranzoni, E.; Cattan, V.; Ghiringhelli, F. Trifluridine/Tipiracil Plus Oxaliplatin Improves PD-1 Blockade in Colorectal Cancer by Inducing Immunogenic Cell Death and Depleting Macrophages. *Cancer Immunol. Res.* **2019**, *7* (12), 1958−1969.

(9) Yu, J.; He, X.; Wang, Z.; Wang, Y.; Liu, S.; Li, X.; Huang, Y. Combining PD-L1 Inhibitors with Immunogenic Cell Death Triggered by Chemo-Photothermal Therapy via a Thermosensitive Liposome System to Stimulate Tumor-Specific Immunological Response. *Nanoscale* **2021**, *13* (30), 12966−12978.

(10) Kepp, O.; Zitvogel, L.; Kroemer, G. Clinical Evidence That Immunogenic Cell Death Sensitizes to PD-1/PD-L1 Blockade. *Oncoimmunology* **2019**, *8* (10), No. e1637188.

(11) Shi, F.; Huang, X.; Hong, Z.; Lu, N.; Huang, X.; Liu, L.; Liang, T.; Bai, X. Improvement Strategy for Immune Checkpoint Blockade:

A Focus on the Combination with Immunogenic Cell Death Inducers. *Cancer Lett.* **2023**, *562*, 216167.
(12) Wang, Q.; Ju, X.; Wang, J.; Fan, Y.; Ren, M.; Zhang, H. Immunogenic Cell Death in Anticancer Chemotherapy and Its Impact on Clinical Studies. *Cancer Lett.* **2018**, *438*, 17−23.
(13) Vanmeerbeek, I.; Sprooten, J.; De Ruysscher, D.; Tejpar, S.; Vandenberghe, P.; Fucikova, J.; Spisek, R.; Zitvogel, L.; Kroemer, G.; Galluzzi, L.; Garg, A. D. Trial Watch: Chemotherapy-Induced Immunogenic Cell Death in Immuno-Oncology. *Oncoimmunology* **2020**, *9* (1), 1703449.
(14) Yamazaki, T.; Buqué, A.; Ames, T. D.; Galluzzi, L. PT-112 Induces Immunogenic Cell Death and Synergizes with Immune Checkpoint Blockers in Mouse Tumor Models. *Oncoimmunology* **2020**, *9* (1), 1721810.
(15) Huang, K.-B.; Wang, F.-Y.; Feng, H.-W.; Luo, H.; Long, Y.; Zou, T.; Chan, A. S. C.; Liu, R.; Zou, H.; Chen, Z.-F.; Liu, Y.-C.; Liu, Y.-N.; Liang, H. An Aminophosphonate Ester Ligand-Containing Platinum(II) Complex Induces Potent Immunogenic Cell Death in Vitro and Elicits Effective Anti-Tumour Immune Responses in Vivo. *Chem. Commun.* **2019**, *55* (87), 13066−13069.
(16) Sun, Y.; Yin, E.; Tan, Y.; Yang, T.; Song, D.; Jin, S.; Guo, Z.; Wang, X. Immunogenicity and Cytotoxicity of a Platinum(IV) Complex Derived from Capsaicin. *Dalton Trans.* **2021**, *50* (10), 3516−3522.
(17) Novohradsky, V.; Markova, L.; Kostrhunova, H.; Kasparkova, J.; Hoeschele, J.; Brabec, V. A [Pt(cis-1,3-diaminocycloalkane)Cl_2] Analog Exhibits Hallmarks Typical of Immunogenic Cell Death Inducers in Model Cancer Cells. *J. Inorg. Biochem.* **2022**, *226*, 111628.
(18) Tham, M. J. R.; Babak, M. V.; Ang, W. H. Platiner: A Highly Potent Anticancer Platinum(II) Complex That Induces Endoplasmic Reticulum Stress Driven Immunogenic Cell Death. *Angew. Chem. Int. Ed.* **2020**, *59* (43), 19070−19078.
(19) Novohradsky, V.; Pracharova, J.; Kasparkova, J.; Imberti, C.; Bridgewater, H. E.; Sadler, P. J.; Brabec, V. Induction of Immunogenic Cell Death in Cancer Cells by a Photoactivated Platinum(IV) Prodrug. *Inorg. Chem. Front.* **2020**, *7* (21), 4150−4159.
(20) Wong, D. Y. Q.; Yeo, C. H. F.; Ang, W. H. Immuno-Chemotherapeutic Platinum(IV) Prodrugs of Cisplatin as Multimodal Anticancer Agents. *Angew. Chem. Int. Ed.* **2014**, *53* (26), 6752−6756.
(21) Wong, D. Y. Q.; Ong, W. W. F.; Ang, W. H. Induction of Immunogenic Cell Death by Chemotherapeutic Platinum Complexes. *Angew. Chem. Int. Ed.* **2015**, *54* (22), 6483−6487.
(22) Groer, C.; Zhang, T.; Lu, R.; Cai, S.; Mull, D.; Huang, A.; Forrest, M.; Berkland, C.; Aires, D.; Forrest, M. L. Intratumoral Cancer Chemotherapy with a Carrier-Based Immunogenic Cell-Death Eliciting Platinum (IV) Agent. *Mol. Pharmaceutics* **2020**, *17* (11), 4334−4345.
(23) Deng, Z.; Wang, N.; Liu, Y.; Xu, Z.; Wang, Z.; Lau, T.-C.; Zhu, G. A Photocaged, Water-Oxidizing, and Nucleolus-Targeted Pt(IV) Complex with a Distinct Anticancer Mechanism. *J. Am. Chem. Soc.* **2020**, *142* (17), 7803−7812.
(24) Bian, M.; Fan, R.; Yang, Z.; Chen, Y.; Xu, Z.; Lu, Y.; Liu, W. Pt(II)-NHC Complex Induces ROS-ERS-Related DAMP Balance to Harness Immunogenic Cell Death in Hepatocellular Carcinoma. *J. Med. Chem.* **2022**, *65* (3), 1848−1866.
(25) Su, X.; Liu, B.; Wang, W.-J.; Peng, K.; Liang, B.-B.; Zheng, Y.; Cao, Q.; Mao, Z.-W. Disruption of Zinc Homeostasis by a Novel Platinum(IV)-Terthiophene Complex for Antitumor Immunity. *Angew. Chem. Int. Ed.* **2023**, *62* (8), No. e202216917.
(26) Ji, S.; Yang, X.; Chen, X.; Li, A.; Yan, D.; Xu, H.; Fei, H. Structure-Tuned Membrane Active Ir-Complexed Oligoarginine Overcomes Cancer Cell Drug Resistance and Triggers Immune Responses in Mice. *Chem. Sci.* **2020**, *11* (34), 9126−9133.
(27) Wang, L.; Guan, R.; Xie, L.; Liao, X.; Xiong, K.; Rees, T. W.; Chen, Y.; Ji, L.; Chao, H. An ER-Targeting Iridium(III) Complex That Induces Immunogenic Cell Death in Non-Small-Cell Lung Cancer. *Angew. Chem. Int. Ed.* **2021**, *60* (9), 4657−4665.
(28) Vigueras, G.; Markova, L.; Novohradsky, V.; Marco, A.; Cutillas, N.; Kostrhunova, H.; Kasparkova, J.; Ruiz, J.; Brabec, V. A Photoactivated Ir(III) Complex Targets Cancer Stem Cells and Induces Secretion of Damage-Associated Molecular Patterns in Melanoma Cells Characteristic of Immunogenic Cell Death. *Inorg. Chem. Front.* **2021**, *8* (21), 4696−4711.
(29) Ling, Y.-Y.; Wang, W.-J.; Hao, L.; Wu, X.-W.; Liang, J.-H.; Zhang, H.; Mao, Z.-W.; Tan, C.-P. Self-Amplifying Iridium(III) Photosensitizer for Ferroptosis-Mediated Immunotherapy against Transferrin Receptor-Overexpressing Cancer. *Small* **2022**, *18* (49), 2203659.
(30) Wang, W.-J.; Ling, Y.-Y.; Zhong, Y.-M.; Li, Z.-Y.; Tan, C.-P.; Mao, Z.-W. Ferroptosis-Enhanced Cancer Immunity by a Ferrocene-Appended Iridium(III) Diphosphine Complex. *Angew. Chem. Int. Ed.* **2022**, *61* (16), No. e202115247.
(31) Wang, L.; Karges, J.; Wei, F.; Xie, L.; Chen, Z.; Gasser, G.; Ji, L.; Chao, H. A Mitochondria-Localized Iridium(III) Photosensitizer for Two-Photon Photodynamic Immunotherapy against Melanoma. *Chem. Sci.* **2023**, *14* (6), 1461−1471.
(32) Ling, Y.-Y.; Kong, Y.-J.; Hao, L.; Pan, Z.-Y.; Mao, Z.-W.; Tan, C.-P. Photodegradation of Carbonic Anhydrase by Iridium Complexes for Induction of Immunogenic Cell Death under Hypoxia. *Inorg. Chem. Front.* **2023**, *10* (11), 3284−3292.
(33) Xiong, X.; Huang, K.-B.; Wang, Y.; Cao, B.; Luo, Y.; Chen, H.; Yang, Y.; Long, Y.; Liu, M.; Chan, A. S. C.; Liang, H.; Zou, T. Target Profiling of an Iridium(III)-Based Immunogenic Cell Death Inducer Unveils the Engagement of Unfolded Protein Response Regulator BiP. *J. Am. Chem. Soc.* **2022**, *144* (23), 10407−10416.
(34) Le, H. V.; Babak, M. V.; Ehsan, M. A.; Altaf, M.; Reichert, L.; Gushchin, A. L.; Ang, W. H.; Isab, A. A. Highly Cytotoxic Gold(I)-Phosphane Dithiocarbamate Complexes Trigger an ER Stress-Dependent Immune Response in Ovarian Cancer Cells. *Dalton Trans.* **2020**, *49* (22), 7355−7363.
(35) Sen, S.; Hufnagel, S.; Maier, E. Y.; Aguilar, I.; Selvakumar, J.; DeVore, J. E.; Lynch, V. M.; Arumugam, K.; Cui, Z.; Sessler, J. L.; Arambula, J. F. Rationally Designed Redox-Active Au(I) N-Heterocyclic Carbene: An Immunogenic Cell Death Inducer. *J. Am. Chem. Soc.* **2020**, *142* (49), 20536−20541.
(36) Mule, R. D.; Kumar, A.; Sancheti, S. P.; Senthilkumar, B.; Kumar, H.; Patil, N. T. BQ-AurIPr: A Redox-Active Anticancer Au(I) Complex That Induces Immunogenic Cell Death. *Chem. Sci.* **2022**, *13* (36), 10779−10785.
(37) Yang, Z.; Bian, M.; Lv, L.; Chang, X.; Wen, Z.; Li, F.; Lu, Y.; Liu, W. Tumor-Targeting NHC−Au(I) Complex Induces Immunogenic Cell Death in Hepatocellular Carcinoma. *J. Med. Chem.* **2023**, *66* (6), 3934−3952.
(38) Xu, Z.; Lu, Q.; Shan, M.; Jiang, G.; Liu, Y.; Yang, Z.; Lu, Y.; Liu, W. NSAID−Au(I) Complexes Induce ROS-Driven DAMPs and Interpose Inflammation to Stimulate the Immune Response against Ovarian Cancer. *J. Med. Chem.* **2023**, *66* (12), 7813−7833.
(39) Lu, Y.; Sheng, X.; Liu, C.; Liang, Z.; Wang, X.; Liu, L.; Wen, Z.; Yang, Z.; Du, Q.; Liu, W. SERD-NHC-Au(I) Complexes for Dual Targeting ER and TrxR to Induce ICD in Breast Cancer. *Pharmacol. Res.* **2023**, *190*, 106731.
(40) Wernitznig, D.; Kiakos, K.; Del Favero, G.; Harrer, N.; Machat, H.; Osswald, A.; Jakupec, M. A.; Wernitznig, A.; Sommergruber, W.; Keppler, B. K. First-in-Class Ruthenium Anticancer Drug (KP1339/IT-139) Induces an Immunogenic Cell Death Signature in Colorectal Spheroids in Vitro. *Metallomics* **2019**, *11* (6), 1044−1048.
(41) Wernitznig, D.; Meier-Menches, S. M.; Cseh, K.; Theiner, S.; Wenisch, D.; Schweikert, A.; Jakupec, M. A.; Koellensperger, G.; Wernitznig, A.; Sommergruber, W.; Keppler, B. K. Plecstatin-1 Induces an Immunogenic Cell Death Signature in Colorectal Tumour Spheroids. *Metallomics* **2020**, *12* (12), 2121−2133.
(42) Konda, P.; Lifshits, L. M.; Roque Iii, J. A.; Cole, H. D.; Cameron, C. G.; McFarland, S. A.; Gujar, S. Discovery of Immunogenic Cell Death-Inducing Ruthenium-Based Photosensitizers for Anticancer Photodynamic Therapy. *Oncoimmunology* **2021**, *10* (1), 1863626.
(43) Xu, Z.; Xu, M.; Wu, X.; Guo, S.; Tian, Z.; Zhu, D.; Yang, J.; Fu, J.; Li, X.; Song, G.; et al. A Half-Sandwich Ruthenium(II) (N^N)

Complex: Inducing Immunogenic Melanoma Cell Death in Vitro and in Vivo. *ChemMedchem* **2023**, *18* (16), No. e202300131.
(44) Su, X.; Wang, W.-J.; Cao, Q.; Zhang, H.; Liu, B.; Ling, Y.; Zhou, X.; Mao, Z.-W. A Carbonic Anhydrase IX (CAIX)-Anchored Rhenium(I) Photosensitizer Evokes Pyroptosis for Enhanced Anti-Tumor Immunity. *Angew. Chem. Int. Ed.* **2022**, *61* (8), No. e202115800.
(45) Wang, F.-X.; Liu, J.-W.; Hong, X.-Q.; Tan, C.-P.; Zhang, L.; Chen, W.-H.; Sadler, P. J.; Mao, Z.-W. Anion-Responsive Manganese Porphyrin Facilitates Chloride Transport and Induces Immunogenic Cell Death. *CCS Chem.* **2022**, *4* (7), 2409−2419.
(46) Kaur, P.; Johnson, A.; Northcote-Smith, J.; Lu, C.; Suntharalingam, K. Immunogenic Cell Death of Breast Cancer Stem Cells Induced by an Endoplasmic Reticulum-Targeting Copper(II) Complex. *ChemBiochem* **2020**, *21* (24), 3618−3624.
(47) Huang, K.-B.; Wang, F.-Y.; Lu, Y.; Yang, L.-M.; Long, N.; Wang, S.-S.; Xie, Z.; Levine, M.; Zou, T.; Sessler, J. L.; Liang, H. Cu(II) Complex That Synergistically Potentiates Cytotoxicity and an Antitumor Immune Response by Targeting Cellular Redox Homeostasis. *Proc. Natl. Acad. Sci. U. S. A.* **2024**, *121* (24), No. e2404668121.
(48) Lu, Y.; Wang, S.-S.; Li, M.-Y.; Liu, R.; Zhu, M.-F.; Yang, L.-M.; Wang, F.-Y.; Huang, K.-B.; Liang, H. Cyclometalated Iridium(III) Complex Based on Isoquinoline Alkaloid Synergistically Elicits the ICD Response and IDO Inhibition via Autophagy-Dependent Ferroptosis. *Acta Pharm. Sin. B* **2025**, *15* (1), 424−437.
(49) Yamazaki, T.; Bravo-San Pedro, J. M.; Galluzzi, L.; Kroemer, G.; Pietrocola, F. Autophagy in the Cancer-Immunity Dialogue. *Adv. Drug Delivery Rev.* **2021**, *169*, 40−50.
(50) Ansari, M. F.; Khan, H. Y.; Tabassum, S.; Arjmand, F. Advances in Anticancer Alkaloid-Derived Metallo-Chemotherapeutic Agents in the Last Decade: Mechanism of Action and Future Prospects. *Pharmacol. Ther.* **2023**, *241*, 108335.
(51) Yang, C.; Mehmood, F.; Lam, T. L.; Chan, S. L.-F.; Wu, Y.; Yeung, C.-S.; Guan, X.; Li, K.; Chung, C. Y.-S.; Zhou, C.-Y.; et al. Stable Luminescent Iridium (III) Complexes with Bis(N-Heterocyclic Carbene) Ligands: Photo-Stability, Excited State Properties, Visible-Light-Driven Radical Cyclization and CO_2 Reduction, and Cellular Imaging. *Chem. Sci.* **2016**, *7* (5), 3123−3136.
(52) Chen, Z.-F.; Qin, Q.-P.; Qin, J.-L.; Liu, Y.-C.; Huang, K.-B.; Li, Y.-L.; Meng, T.; Zhang, G.-H.; Peng, Y.; Luo, X.-J.; Liang, H. Stabilization of G-Quadruplex DNA, Inhibition of Telomerase Activity, and Tumor Cell Apoptosis by Organoplatinum(II) Complexes with Oxoisoaporphine. *J. Med. Chem.* **2015**, *58* (5), 2159−2179.
(53) Qiu, X.; Qu, Y.; Guo, B.; Zheng, H.; Meng, F.; Zhong, Z. Micellar Paclitaxel Boosts ICD and Chemo-Immunotherapy of Metastatic Triple Negative Breast Cancer. *J. Control. Release* **2022**, *341*, 498−510.
(54) Nielsen, T. O.; Leung, S. C. Y.; Rimm, D. L.; Dodson, A.; Acs, B.; Badve, S.; Denkert, C.; Ellis, M. J.; Fineberg, S.; Flowers, M.; Kreipe, H. H.; Laenkholm, A.-V.; Pan, H.; Penault-Llorca, F. M.; Polley, M.-Y.; Salgado, R.; Smith, I. E.; Sugie, T.; Bartlett, J. M. S.; McShane, L. M.; Dowsett, M.; Hayes, D. F. Assessment of Ki67 in Breast Cancer: Updated Recommendations from the International Ki67 in Breast Cancer Working Group. *J. Natl. Cancer Inst.* **2021**, *113* (7), 808−819.
(55) Wu, P.; Zhao, L.; Chen, Y.; Xin, Z.; Lin, M.; Hao, Z.; Chen, X.; Chen, D.; Wu, D.; Chai, Y. CD38 Identifies Pre-activated $CD8^+$ T Cells Which Can Be Reinvigorated by Anti-PD-1 Blockade in Human Lung Cancer. *Cancer Immunol., Immunother.* **2021**, *70* (12), 3603−3616.
(56) Wang, Q.; Qin, Y.; Li, B. $CD8^+$ T Cell Exhaustion and Cancer Immunotherapy. *Cancer Lett.* **2023**, *559*, 216043.
(57) Okła, K.; Farber, D. L.; Zou, W. Tissue-Resident Memory T Cells in Tumor Immunity and Immunotherapy. *J. Exp. Med.* **2021**, *218* (4), No. e20201605.
(58) Speiser, D. E.; Chijioke, O.; Schaeuble, K.; Münz, C. $CD4^+$ T Cells in Cancer. *Nature Cancer* **2023**, *4* (3), 317−329.
(59) Tie, Y.; Tang, F.; Wei, Y.-Q.; Wei, X.-W. Immunosuppressive Cells in Cancer: Mechanisms and Potential Therapeutic Targets. *J. Hematol. Oncol.* **2022**, *15* (1), 61.
(60) Franken, H.; Mathieson, T.; Childs, D.; Sweetman, G. M. A.; Werner, T.; Tögel, I.; Doce, C.; Gade, S.; Bantscheff, M.; Drewes, G.; Reinhard, F. B. M.; Huber, W.; Savitski, M. M. Thermal Proteome Profiling for Unbiased Identification of Direct and Indirect Drug Targets Using Multiplexed Quantitative Mass Spectrometry. *Nat. Protoc.* **2015**, *10* (10), 1567−1593.
(61) Savitski, M. M.; Reinhard, F. B. M.; Franken, H.; Werner, T.; Savitski, M. F.; Eberhard, D.; Molina, D. M.; Jafari, R.; Dovega, R. B.; Klaeger, S.; et al. Tracking Cancer Drugs in Living Cells by Thermal Profiling of the Proteome. *Science* **2014**, *346* (6205), 1255784.
(62) Seo, S. U.; Woo, S. M.; Min, K.-J.; Kwon, T. K. Itch and Autophagy-Mediated NF-κB Activation Contributes to Inhibition of Cathepsin D-Induced Sensitizing Effect on Anticancer Drugs. *Cell Death Dis.* **2022**, *13* (6), 552.
(63) Singh, S.; Maurya, A. K.; Meena, A.; Mishra, N.; Luqman, S. Myricitrin from Bayberry as a Potential Inhibitor of Cathepsin-D: Prospects for Squamous Lung Carcinoma Prevention. *Food Chem. Toxicol.* **2023**, *179*, 113988.
(64) Zuhl, A. M.; Nolan, C. E.; Brodney, M. A.; Niessen, S.; Atchison, K.; Houle, C.; Karanian, D. A.; Ambroise, C.; Brulet, J. W.; Beck, E. M.; et al. Chemoproteomic Profiling Reveals That Cathepsin D Off-Target Activity Drives Ocular Toxicity of β-Secretase Inhibitors. *Nat. Commun.* **2016**, *7* (1), 13042.
(65) Martins, I.; Wang, Y.; Michaud, M.; Ma, Y.; Sukkurwala, A. Q.; Shen, S.; Kepp, O.; Métivier, D.; Galluzzi, L.; Perfettini, J. L.; Zitvogel, L.; Kroemer, G. Molecular Mechanisms of ATP Secretion During Immunogenic Cell Death. *Cell Death Differ.* **2014**, *21* (1), 79−91.
(66) Fucikova, J.; Kepp, O.; Kasikova, L.; Petroni, G.; Yamazaki, T.; Liu, P.; Zhao, L.; Spisek, R.; Kroemer, G.; Galluzzi, L. Detection of Immunogenic Cell Death and Its Relevance for Cancer Therapy. *Cell Death Dis.* **2020**, *11* (11), 1013.
(67) Michaud, M.; Martins, I.; Sukkurwala, A. Q.; Adjemian, S.; Ma, Y.; Pellegatti, P.; Shen, S.; Kepp, O.; Scoazec, M.; Mignot, G.; Rello-Varona, S.; Tailler, M.; Menger, L.; Vacchelli, E.; Galluzzi, L.; Ghiringhelli, F.; di Virgilio, F.; Zitvogel, L.; Kroemer, G. Autophagy-Dependent Anticancer Immune Responses Induced by Chemotherapeutic Agents in Mice. *Science* **2011**, *334* (6062), 1573−1577.
(68) Suter, D. M. Transcription Factors and DNA Play Hide and Seek. *Trends Cell. Biol.* **2020**, *30* (6), 491−500.
(69) Anthony, E. J.; Bolitho, E. M.; Bridgewater, H. E.; Carter, O. W. L.; Donnelly, J. M.; Imberti, C.; Lant, E. C.; Lermyte, F.; Needham, R. J.; Palau, M.; Sadler, P. J.; Shi, H.; Wang, F.-X.; Zhang, W.-Y.; Zhang, Z. Metallodrugs Are Unique: Opportunities and Challenges of Discovery and Development. *Chem. Sci.* **2020**, *11* (48), 12888−12917.

https://doi.org/10.1021/jacs.5c00255
J. Am. Chem. Soc. 2025, 147, 15216−15228